Accepted Manuscript

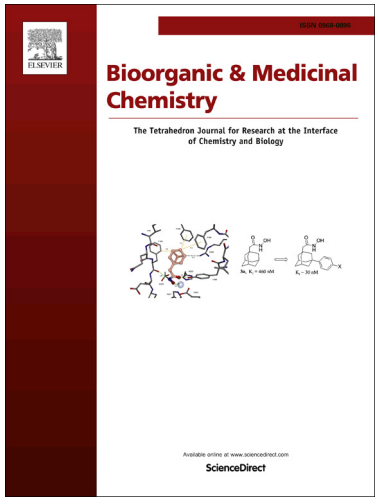

Targeting zoonotic viruses: structure-based inhibition of the 3C-like protease from bat coronavirus HKU4 – the likely reservoir host to the human coronavirus that causes Middle East Respiratory Syndrome (MERS)

Sarah E. St. John, Sakshi Tomar, Shaun R. Stauffer, Andrew D. Mesecar

PII: S0968-0896(15)00533-7
DOI: http://dx.doi.org/10.1016/j.bmc.2015.06.039
Reference: BMC 12395

To appear in: *Bioorganic & Medicinal Chemistry*

Received Date: 16 April 2015
Revised Date: 2 June 2015
Accepted Date: 10 June 2015

Please cite this article as: St. John, S.E., Tomar, S., Stauffer, S.R., Mesecar, A.D., Targeting zoonotic viruses: structure-based inhibition of the 3C-like protease from bat coronavirus HKU4 – the likely reservoir host to the human coronavirus that causes Middle East Respiratory Syndrome (MERS), *Bioorganic & Medicinal Chemistry* (2015), doi: http://dx.doi.org/10.1016/j.bmc.2015.06.039

Targeting zoonotic viruses: structure-based inhibition of the 3C-like protease from bat coronavirus HKU4 – the likely reservoir host to the human coronavirus that causes Middle East Respiratory Syndrome (MERS).

Sarah E. St. John,[1,2,3] Sakshi Tomar,[1,3] Shaun R. Stauffer,[4] and Andrew D. Mesecar[1,2,3]*

[1]Department of Biological Sciences, Purdue University, West Lafayette, Indiana, USA
[2]Department of Chemistry, Purdue University, West Lafayette, Indiana, USA
[3]Centers for Cancer Research & Drug Discovery, Purdue University, West Lafayette, Indiana, USA
[4]Department of Pharmacology, Department of Chemistry, Vanderbilt University Medical Center, Nashville, Tennessee, USA

*Corresponding Author's Contact Information:
Andrew D. Mesecar, Ph.D.
Professor, Departments of Biological Sciences and Chemistry
Purdue University
915 West State Street
West Lafayette, Indiana 47907
Ph: 765-494-1924
Email: amesecar@purdue.edu

Summary

The bat coronavirus HKU4 belongs to the same 2c lineage as that of the deadly Middle East Respiratory Syndrome coronavirus (MERS-CoV) and shows high sequence similarity, therefore potentiating a threat to the human population through a zoonotic shift or "spill over" event. To date, there are no effective vaccines or antiviral treatments available that are capable of limiting the pathogenesis of any human coronaviral infection. An attractive target for the development of anti-coronaviral therapeutics is the 3C-like protease ($3CL^{pro}$), which is essential for the progression of the coronaviral life cycle. Herein, we report the screening results of a small, 230-member peptidomimetic library against HKU4-CoV $3CL^{pro}$ and the identification of 43 peptidomimetic compounds showing good to excellent inhibitory potency of HKU4-CoV $3CL^{pro}$ with IC_{50} values ranging from low micromolar to sub-micromolar. We established structure-activity relationships (SARs) describing the important ligand-based features required for potent HKU4-CoV $3CL^{pro}$ inhibition and identified a seemingly favored peptidic backbone for HKU4-CoV $3CL^{pro}$ inhibition. To investigate this, a molecular sub-structural analysis of the most potent HKU4-CoV $3CL^{pro}$ inhibitor was accomplished by the synthesis and testing of the lead peptidomimetic inhibitor's sub-structural components, confirming the activity of the favored backbone (**22A**) identified via SAR analysis. In order to elucidate the structural reasons for such potent HKU4-CoV $3CL^{pro}$ inhibition by the peptidomimetics having the **22A** backbone, we determined the X-ray structures of HKU4-CoV $3CL^{pro}$ in complex with three peptidomimetic inhibitors. Sequence alignment of HKU4-CoV $3CL^{pro}$, and two other lineage C *Betacoronaviruses* $3CL^{pro}$'s,

HKU5-CoV and MERS-CoV 3CL^{pro}, show that the active site residues of HKU4-CoV 3CL^{pro} that participate in inhibitor binding are conserved in HKU5-CoV and MERS-CoV 3CL^{pro}. Furthermore, we assayed our most potent HKU4-CoV 3CL^{pro} inhibitor for inhibition of HKU5-CoV 3CL^{pro} and found it to have sub-micromolar inhibitory activity (IC_{50} = 0.54 ± 0.03 μM). The X-ray structures and SAR analysis reveal critical insights into the structure and inhibition of HKU4-CoV 3CL^{pro}, providing fundamental knowledge that may be exploited in the development of anti-coronaviral therapeutics for coronaviruses emerging from zoonotic reservoirs.

1. Introduction

Zoonotic viruses, including coronaviruses, Ebola virus, HIV, influenza A viruses, hantaviruses or henipaviruses, are ubiquitous and can emerge as significant human pathogens capable of global epidemics and pandemics. Most often, we spend our time and resources in targeting only the human pathogens with small molecule inhibitors with the ultimate goal of developing therapeutic compounds to treat the associated diseases. A missed opportunity, however, is targeting the zoonotic host with small molecule inhibitors with the goal of utilizing the acquired chemical and structural knowledge to inform us of the evolutionary path of the virus on a biological basis. So, we believe that by using small molecule compounds as probes of the structural evolution of viral enzyme drug targets, from the zoonotic reservoirs to the human pathogens, we can gain new insights and predict a priori the structural scaffolds of small molecule compounds that can serve as lead templates for therapeutic development against emerging human pathogenic viruses such as coronaviruses.

Coronaviruses (CoVs) are enveloped, single-stranded, positive-sense RNA viruses that infect and cause disease in a variety of species including bats, birds, cats, dogs, pigs, mice, horses, whales, and humans.[1-3] Coronaviral infections may range from mild to severe and can result in respiratory, enteric, hepatic, or neurological diseases in their carriers. The first two human CoV strains (HCoV-229E and HCoV-OC43) were identified in the mid-1960s, and it wasn't until the 21st century that a new human coronavirus (Severe Acute Respiratory Syndrome or SARS-CoV) was identified.[4,5] Currently, there are at least six known human CoVs including: HCoV-229E, HCoV-NL63, HCoV-OC43, HCoV-HKU1, SARS-CoV, and most recently, the Middle East respiratory syndrome coronavirus (MERS-CoV).[6] MERS-CoV, formerly known as HCoV-EMC, was identified in November 2012, when it was isolated from the sputum a 60-year-old Saudi Arabian man presenting acute pneumonia and renal failure.[7] Since the time of its identification, the virus has grown to be a threat to public health worldwide having a case-fatality rate of about 30%.[8] To date, there are no vaccines or antiviral agents capable of preventing or treating any human coronaviral infection.

MERS-CoV belongs to lineage C in the genus *Betacoronavirus* of the *Coronaviridae* family in the *Nidovirales* order.[9] Also of this lineage are the species *Tylonycteris* bat coronavirus HKU4 (HKU4-CoV) and *Pipistrellus* bat coronavirus HKU5 (HKU5-CoV), where the overall amino acid sequence identities of MERS-CoV to HKU4-CoV and HKU5-CoV across the conserved domains are approximately 75% and 76.7%, respectively.[6,10,11] Though the exact origin of MERS-CoV is currently debated, a bat origin is strongly suspected as MERS-CoV is so closely related to HKU4- and HKU5-CoV and because MERS-CoV genomic RNA has been found in bats and dromedary camels in Qatar.[12,13] Though HKU4-CoV and HKU5-CoV have been found only in bats, studies have shown that their accessory proteins are capable of inhibiting human antiviral signaling pathways *in vitro*.[14,15] This, and the close similarity of MERS-CoV to HKU4-CoV and HKU5-CoV, suggests that a zoonotic shift from bats or camels to humans may have occurred.[15] A recent investigation into the interactions between the human CD26 receptor and the receptor binding domains (RBDs) in the MERS-CoV, HKU4-CoV and HKU5-CoV envelope-embedded spike protein revealed that MERS-CoV and HKU4-CoV both engage this receptor for viral entry whereas HKU5-CoV does not.[16] These observations suggest that an evolutionary pathway from bat HKU4-CoV to human MERS-CoV exists and that investigating the molecular basis of this zoonotic shift from a structural and chemical-biology perspective may allow us to predict and target the these viruses with small molecule therapeutics.

Coronaviral genomes are polycistronic, encoding for two large polyproteins, pp1a and pp1ab.[17-20] Initiation of coronavirus replication in cells occurs by the translation of two overlapping, open reading frames (ORF1a and ORF1b) to produce pp1a and, following a -1 ribosomal frameshift mechanism, pp1ab. These polyproteins are then proteolytically processed at 14 cleavage sites by two essential viral cysteine proteases, the papain-like protease (PL^{pro}, or nsp3) and the 3C-like protease ($3CL^{pro}$, also known as the main protease, M^{pro}, or nsp5). Cleavage by both proteases results in the production of 16 nonstructural proteins (nsps), where PL^{pro} is responsible for cleavage at 3 sites and $3CL^{pro}$ is responsible for cleavage at 11 sites (Figure 1). The function of $3CL^{pro}$ is vital for the coronaviral life cycle, making it an attractive target for the development of antiviral drugs.[21,22]

The present work was undertaken to investigate the kinetic and structural properties of HKU4-CoV $3CL^{pro}$ and to utilize this knowledge to discover and develop potent inhibitors of HKU4-CoV $3CL^{pro}$. Targeting the immediate zoonotic reservoirs of coronaviruses with small molecule inhibitors can help inform structure-based design strategies aimed at creating molecular scaffolds that may also target the emerging human CoVs and ultimately aid in the development of therapeutics against coronaviral infection. Towards this goal, we first expressed, purified, and characterized the kinetic properties of HKU4-CoV $3CL^{pro}$. We then determined the inhibition of HKU4-CoV 3CLpro by a small library of 230 peptidomimetic compounds, which resulted in the identification of 43 HKU4-CoV

3CLpro inhibitors, two of which showed sub-micromolar potency. With a potent lead inhibitor compound in hand, we investigated the contributions of its individual sub-structural components to inhibitory potency and identified a favored peptidic backbone for HKU4-CoV 3CL^{pro} inhibition. Finally, we determined the X-ray crystal structures of the three most potent inhibitors containing this favored backbone in complex with HKU4-CoV 3CL^{pro} and elucidated the structural reasons behind such potent HKU4-CoV 3CL^{pro} inhibition.

2. Results and Discussion

2.1. Screen of peptidomimetic library for HKU4-CoV 3CL^{pro} inhibition

A library of 230 previously reported, peptidomimetic-type compounds[23,24] was screened for inhibition of HKU4-CoV 3CL^{pro} at a single concentration of 100 μM, and IC_{50} values were determined for compounds that showed greater than 50% inhibition of HKU4-CoV 3CL^{pro} at that concentration. This screen resulted in the identification of 43 peptidomimetic compounds with inhibitory concentrations ranging from micromolar to sub-micromolar (*vide infra*). The peptidomimetic inhibitors can be grouped into two classes, inhibitors with a single amide bond in the inhibitor backbone (Class A) and inhibitors with a dipeptide-like backbone (Class B). The results of this screen are displayed in Table 1a (Class A) and Table 1b (Class B), where only the compounds that showed greater than 50% inhibition of HKU4-CoV 3CL^{pro} at 100 μM are shown (see Supporting Information S1 and S2 for comprehensive list of compounds tested). The compounds are listed in the tables in rank order by IC_{50} values starting with the lowest IC_{50} value. Of the 25 Class A inhibitors that were tested for inhibition of HKU4-CoV 3CL^{pro}, 19 were found to inhibit HKU4-CoV 3CL^{pro} above 50% at a concentration of 100 μM, and subsequently, IC_{50} values were determined. Remarkably, the two most potent inhibitors, **1A** and **2A**, proved to be sub-micromolar inhibitors of HKU4-CoV 3CL^{pro}, having IC_{50}'s of 0.33 ± 0.02 and 0.41 ± 0.04 μM, respectively. Upon examination of all 27 Class A inhibitors, an immediate trend is apparent where there is an overwhelming preference for a 3-thiophene at the R_1 position and a 1-methylbenzotriazole at the R_3 position of the peptidomimetic backbone. This is observed in every Class A inhibitor found to produce inhibition of HKU4-CoV 3CL^{pro} over 50% at 100 μM, with the exception of the least active analogue in this series, **19A**. **19A** only differs from the more active compound **6A** in that **19A** has a triazole in place of a benzotriazole; however, this difference is significant enough to decrease inhibitory potency ten-fold between the analogues, from 1.6 ± 0.1 μM for **6A** to 16.0 ± 4.0 μM for **19A**. Interestingly, **19A** maintains a triazole ring in the R_3 position, indicating that the position of the nitrogen atoms in this heterocycle is essential for good HKU4-CoV 3CL^{pro} inhibition. Other R_3 heterocycles incorporated in the less active members of Class A include 4-

substituted methyltriazoles, 4-imidazoles, and 2-furans, underscoring the importance of the methylbenzotriazole at the R_3 position and pointing to the potential significance of a precisely oriented hydrogen bond acceptor (see Supporting information S1 for a comprehensive list).

Of the 19 Class A peptidomimetics found to be good inhibitors of HKU4-CoV $3CL^{pro}$, 13 have amide substituents at R_2, four have aromatics (**5A**, **7A**, **9A**, and **11A**), and two have amines (**16A** and **17A**). Among the inhibitors with amide substituents at R_2, a trend can be observed where cyclic carboxamides are preferred (**1A**, **2A**, **3A**, **4A**, and **8A**) to alkyl carboxamides, with the aromatic carboxamides being the most active (**1A** and **2A**). A preference for larger cyclic carboxamides is also observed, where 4, 5 or 6 membered cycles (**1A**, **2A**, **3A**, and **4A**) are preferred over the smaller cyclopropylcarboxamide (**8A**).

Among the six Class A inhibitors with aromatic groups substituted at the R_2 position (**5A**, **7A**, **9A**, **11A**, **20A**, **21A**), only the four compounds **5A, 7A, 9A** and **11A** were found to inhibit HKU4-CoV $3CL^{pro}$ above 50% at 100 μM and they each contain aromatic nitrogen heterocycles. The position of the nitrogen is of moderate significance, as a *p*-substituted pyridine at R_2 is 2-fold more active than the *m*-substituted pyridine (**5A** vs. **11A**, Table 1a). Bulky substituents on R_2 aromatic heterocycles, such as in **20A**, decrease inhibition of HKU4-CoV $3CL^{pro}$, indicating a steric requirement within the R_2 binding pocket (Table 1a and S1). Interestingly, **20A** is one of only two Class A compound having a 3-thiophene at the R_1 position and a 1-methylbenzotriazole at the R_3 position that is not a good inhibitor of HKU4-CoV 3CLpro at 100 μM. Addition of a methoxy substituent to the R_2 heterocycle is tolerated (**7A** and **9A,** Table 1a), but does not increase or decrease inhibition significantly, indicating that the addition of another hydrogen-bond acceptor does not further engage the R_2 binding pocket and that smaller aromatic substituents can be tolerated.

The two Class A peptidomimetics that have R_2 amines, **16A** and **17A**, have similar IC_{50} values (4.8 ± 0.4 and 5.3 ± 0.6 μM, respectively); however, they have vastly different steric requirements (methyl vs. benzyl). As opposed to the R_2 amides and aromatics, this may indicate that when an amine substituent is present at the R_2 position, it dictates an alternative binding orientation within the R_2 binding space that does not lead to such strict steric requirements. Alternatively, the relatively hydrophobic benzyl group of **17A** may decrease inhibitor solubility and consequent inhibitor availability, therefore resulting in lower % maximum inhibition and IC_{50} value than would otherwise be observed. This may also be the case for **21A**, where the R_2 aromatic ring lacks the nitrogen found in the more active inhibitors **5A** and **11A** (Table 1a and S1).

A comparison of **17A** to the second most active inhibitor in Class A, **2A**, which is only different from **17A** by the presence of a carbonyl, shows that the carbonyl of **2A** is crucial for sub-micromolar

inhibitory potency (0.41 ± 0.04 μM for **2A** vs. 5.3 ± 0.6 μM for **17A**). This observed 10-fold increase in IC_{50} may be a consequence of the loss of a stabilizing hydrogen-bond interaction between the amide –NH group or carbonyl oxygen of the inhibitor and the HKU4-CoV $3CL^{pro}$ binding site. The change in hybridization between an amine and an amide also results in a change in the molecular geometry of the R_2 substituent, which may alter hydrogen-bonding properties and introduce additional effects that may be important factors in dictating good enzymatic inhibition. The X-ray structure of HKU4-CoV $3CL^{pro}$ in complex with **2A,** discussed below, shows that the amide –NH group of the carboxamide group of **2A** forms an important interaction with the backbone carbonyl of His41.

Of the 205 Class B inhibitors that were tested for inhibition of HKU4-CoV $3CL^{pro}$, 24 were found to inhibit HKU4-CoV $3CL^{pro}$ above 50% at a concentration of 100 μM, and subsequently, IC_{50} values were determined (Table 1b). Interestingly, we found fewer good inhibitors and no sub-micromolar inhibitors of HKU4-CoV $3CL^{pro}$ among this larger, more substituted dipeptide-like class of compounds (~76% of compounds in Class A (19 of 25 compounds tested) were good inhibitors of HKU4-CoV $3CL^{pro}$ while only ~12% of compounds in Class B (24 of 205 compounds tested) were found to be good inhibitors). This result could be a consequence of the increased steric bulk perturbing the preferred binding orientation of the Class B compounds in the HKU4-CoV $3CL^{pro}$ binding site. A comparison of similar Class A and Class B inhibitors more clearly elucidates this trend, where the addition of the sterically bulky R_4 *t*-Bu amide in the Class B compounds decreases HKU4-CoV $3CL^{pro}$ inhibition in each instance (S3). For example, the most active Class A inhibitor, **1A**, having and IC_{50} of 0.33 ± 0.02 μM and 93% inhibition at 100 μM, is almost completely inactivated by the addition of the *t*-Bu amide as seen in the Class B compound **25B**, with only 26% inhibition at 100 μM. Within the Class B inhibitors, there is a preference for the 3-thiophene at the R_1 position and a 1-methylbenzotriazole at the R_3 position of the peptidomimetic backbone, though it is not as strong as that observed in within Class A (25% of compounds in Class B vs. 95% of compounds in Class A). Among the series where R_1 = 3-thiophene and R_3 = 1-methylbenzotriazole (compounds **3B**, **6B**, **9B**, **16B**, **18B**, and **21B**) small carboxamide groups at the R_2 position are favored as observed by the comparison of **3B** to **28B** and **6B** to **27B** (see Tables 2 and 3). Possibly, Class B inhibitors with small R_2 amides allow for a shift in the position of the inhibitor in the HKU4-CoV $3CL^{pro}$ binding site to accommodate the bulky t-Bu amide at the R_4 position. Again, an R_2 amide is preferred to an amine for good inhibition of HKU4-CoV $3CL^{pro}$ (IC_{50} = 1.8 ± 0.5 μM for **3B** vs. 22.0 ± 7.4 μM for **21B**). Replacement of the benzotriazole within this series with a benzimidazole has dissimilar effects; for example, comparing **19B** (Table 1b) to **28B** (S2 and S3) where the benzimidazole of **19B** has been replaced with a benzotriazole, inhibition decreases from 68% to 34% at 100 μM, respectively. In

contrast, comparison of **23B** to **18B** shows that substitution of benzimidazole for benzotriazole increases inhibition from 56% to 76% at 100 μM (Table 1b). Interestingly, only Class B compounds having a *para*-substituted phenyl ring with an R_2 substituent were found to be good inhibitors of HKU4-CoV $3CL^{pro}$; compounds with other, non-phenyl rings including cyclopropyl, cyclohexyl, adamantane, and bicycloheptane were not found to be active inhibitors.

2.2. 1A-RFL Sub-structural activity analysis via component synthesis

In an attempt to delineate the structural relationships that contribute to the enhanced activity of our most active inhibitor, **1A**, we accomplished the synthesis of the sub-structural components of **1A** and determined their individual inhibitory activities against HKU4-CoV $3CL^{pro}$ (Scheme 1). The straightforward synthesis of these sub-structural **1A** components, **22A**, **23A**, and **24A**, was accomplished from the commercially available starting materials, benzotriazole and *p*-phenylenediamine. The synthesis of **22A** was achieved in two steps. First, alkylation of benzotriazole by reaction with chloroacetic acid and sodium hydroxide yielded the benzotriazoleacetic acid **22** in 50% yield.[25] Subsequent coupling of **22** with the commercially available thiophenylmethanamine using EDC produced the desired **1A** component **22A** in 25% yield (Scheme 1, top). The synthesis of **23A** and **24A** was accomplished linearly by first coupling *p*-phenylenediamine with the commercially available thiophenecarboxylic acid using HATU, which resulted in the desired **1A** component **23A** in 58% yield. Reductive amination of **23A** and commercially available thiophenecarbaldehyde using sodium triacetoxyborohydride produced the desired **1A** sub-structural component **24A** in 81% yield. Finally, **1A** was resynthesized according to the literature procedure by coupling **24A** with **22** using EDC as a coupling reagent.[24]

The sub-structural components **22A**, **23A**, and **24A** were then individually tested for inhibition of HKU4-CoV $3CL^{pro}$ at a concentration of 100 μM. The **22A** component, representing the R_1 and R_3 substituents of the Class A peptidomimetic backbone, showed 28% inhibition of HKU4-CoV $3CL^{pro}$ at 100 μM and had an IC_{50} of 68 μM, supporting our hypothesis that this backbone has some inhibitory capacity even in the absence of the R_2 component. The **23A** sub-structural component, representing the R_2 substituent of the Class A peptidomimetic backbone, was found to have no inhibitory activity against HKU4-CoV $3CL^{pro}$ at 100 μM, supporting R_1 and R_3 as essential substituents. Additionally, the **24A** sub-structural component, representing the R_1 and R_2 substituents of the Class A peptidomimetic backbone, showed no inhibition of HKU4-CoV $3CL^{pro}$ at 100 μM, indicating the crucial nature of the 1-methylbenzotriazole at the R_3 position of the Class A backbone and supporting our previous observation of the need for a precisely oriented hydrogen bond acceptor at this position within the

Class A peptidomimetics (*vide supra*). This finding establishes **22A** as a minimum component necessary for inhibition of HKU4-CoV 3CL^{pro} and suggests it may be used as a scaffold for future fragment based design of HKU4-CoV 3CL^{pro} inhibitors. Interestingly, the work of Wong and coworkers showed that a series of benzotriazole esters, which act as potent, covalent inhibitors of SARS-3CL^{pro}, are also able to inhibit SARS-3CL^{pro} upon replacement of the ester oxygen with carbon, albeit weakly.[26] Taken together, these findings may indicate an inhibitory preference for benzotriazoles among coronaviral 3C-like proteases.

2.3. X-ray crystallographic analysis of HKU4-CoV 3CL^{pro} in complex with 1A, 2A, and 3B.

In order to more fully elucidate the structural factors underlying the structure-activity relationships (SARs) observed in the kinetic data, we determined the X-ray crystal structures of HKU4-CoV 3CL^{pro} in complex with three of the most potent inhibitors, **1A**, **2A**, **3B** and the favored backbone **22A**. These complexes were chosen to determine the potential structural explanations behind our observations that Class A and B inhibitor backbones, containing a 3-thiophene and 1-methylbenzotriazole, are favored for HKU4-CoV 3CL^{pro} inhibition. We also sought to determine the structural reasons behind the preference for inhibition by Class A compounds over Class B compounds.

Co-crystallization of **1A**, **2A**, **3B**, and **22A** with HKU4-CoV 3CL^{pro} produced high-quality crystals suitable for X-ray data collection and structure determination. Complete X-ray data sets were collected on these four HKU4-CoV 3CL^{pro}-inhibitor complexes to resolutions between 1.8 Å and 2.3 Å. A summary of the data collection and refinement statistics are provided in S4.

The X-ray crystal structures confirm that both the Class A (**1A** and **2A**) and B (**3B**) peptidomimetics bind in the active site pocket of HKU4-Co 3CL^{pro}, which is lined primarily with polar residues and is solvent exposed (Figure 2). In each of the HKU4-CoV 3CL^{pro}-inhibitor complexes, the carbonyl carbon of the central inhibitor backbone, i.e preceding the R_3 group, is located between 4.5-4.8 Å from the sulfur atom of the catalytic cysteine (Cys148, Figure 2, A, C, E). Both **1A** and **2A**, which have a 3-thiophene at the R_1 position and a 1-methylbenzotriazole at the R_3 position of the peptidomimetic backbone, position these moieties in identical chemical space (Figure 2, A & C). The Class B inhibitor, **3B**, which has a 3-thiophene at the R_1 position and a 1-methylbenzotriazole at the R_3 position, also positions the 3-thiophene and 1-methylbenzotriazole functionalities in the same chemical space utilized by the Class A inhibitors (Figure 2, E). The 3-thiophene in the R_1 position of all three inhibitors occupies the S_2-S_4 sub-sites of the HKU4-CoV 3CL^{pro} active site, the anilido and R_2-functionality reside in the S_2-S_1' sub-sites, and the R_3 benzotriazole occupies the S_1-subsite, acting as the P_1 group of the substrate.

The X-ray structures reveal the structural determinants for the inhibitory preference for Class A and B compounds with backbones containing a 3-thiophene and 1-methylbenzotriazole. This backbone allows the inhibitor to anchor into the HKU4-CoV 3CL^{pro} active site via the formation of three key hydrogen bonds. First, there is a direct hydrogen bond that exists between the 3-nitrogen atom of benzotriazole and the *tele*-nitrogen of His166 in each enzyme-inhibitor complex, securing the location and position of the benzotriazole in the active site. A second hydrogen bond between the carbonyl oxygen of the inhibitor backbone and the backbone nitrogen of Glu169 in each structure further anchors the inhibitor in the HKU4-CoV 3CL^{pro} active site. Finally, the thiophene ring is positioned within the HKU4-CoV 3CL^{pro} active site allowing the formation of a relatively uncommon hydrogen bond to the hydroxyl hydrogen of Tyr54.[27-30]

In each of the HKU4-CoV 3CL^{pro}-inhibitor complexes, the R_2-substituted aryl ring of both Class A and B inhibitors is positioned in the HKU4-CoV 3CL^{pro} active site to take advantage of an edge-to-face pi-interaction with the catalytic histidine, His41 (Figure 2, A, C, E). This interaction is may be important for good inhibition of HKU4-CoV 3CL^{pro} for two reasons. First, comparing **1A** and **2A** to **22A**, where the R_2-substituted aromatic ring of **1A** and **2A** is absent, a greater than 200-fold increase in IC_{50} is observed for **22A**. Second, Class B compounds having non-aromatic substituents instead of an R_2-substituted aryl ring were not found to be good inhibitors of HKU4-CoV 3CL^{pro} (*vide supra*). These data indicate that for low micromolar to sub-micromolar inhibition of HKU4-CoV 3CL^{pro}, an R_2-substituted aryl ring may be required. Furthermore, there is a conserved active site water molecule present in the X-ray crystal structure of each HKU4-CoV 3CL^{pro}-inhibitor complex that mediates a hydrogen-bond between the backbone carbonyl oxygen of His41 and the amide R_2 nitrogen of the inhibitor (Figure 2, A, C, E). This finding illuminates the observed preference for an amide substituent at the R_2 position in both Class A and B inhibitors.

Our attempt to solve the X-ray crystal structure of **22A** in complex with HKU4-CoV 3CL^{pro} did not result in the structure of the HKU4-CoV 3CL^{pro}-inhibitor complex, but instead resulted in the X-ray structure of the unliganded, or free, HKU4-CoV 3CL^{pro} enzyme, which was found to crystallize in a different space group than the HKU4-CoV 3CL^{pro}-inhibitor complexes (Figure 3, A). The unbound, or free, HKU4-CoV 3CL^{pro} enzyme was found to have noteworthy changes in the active site architecture in comparison to the X-ray crystal structures of the HKU4-CoV 3CL^{pro}-inhibitor complexes. In the absence of an inhibitor, what appears to be a metal ion binds to the HKU4-CoV 3CL^{pro} active site by coordinating to the catalytic cysteine (Cys148), which is rotated 180° from the inhibitor bound structures, resulting in a 3.2 Å positional change in the location of the sulfur atom with a distance of 2.2 Å between the sulfur of Cys148 and the metal atom. The metal is presumed to be a zinc cation, as it is present in water and likely to bind to a sulfur atom (also seen in PDB ID 2YNA), though it could

also be iron. The *tele*-nitrogen of His41 is shifted 2.6 Å from its position in the HKU4-CoV 3CL^{pro}-**1A-RFL** complex X-ray crystal structure, allowing for the coordination of the Zn^{2+} atom, which is located 2.4 Å away (Figure 3, A). Additionally, the positions of the Met25, Cys44, Ala46, Tyr54, and Gln192 residues all noticeably shift upon superposition of the free and inhibitor-bound forms of HKU4-CoV 3CL^{pro}.

Comparing the most potent Class B inhibitor having the 1-methylbenzotriazole and 3-thiophene backbone, **3B**, to the top HKU4-CoV 3CL^{pro} inhibitor identified, **1A**, elucidates the observed preference for Class A inhibitors over Class B inhibitors (Figure 3, C). The (*R*)-enantiomer of the Class B compound, **3B**, was found in the HKU4-CoV 3CL^{pro} active site, with the backbone of the inhibitor oriented similarly to the backbones of the Class A inhibitors **1A** and **2A**, utilizing the same hydrogen bonds; however, the (*R*)-R_4 *t*-Bu amide substituent of **3B**, which is absent in the Class A inhibitors, marginally rotates the thiophene away from Tyr54, increasing the distance to the hydrogen-bond donor Tyr54 from 3.9 to 4.5 Å compared to **1A**, and moving the thiophene out of hydrogen-bonding distance to Tyr54 (distance measured to heteroatoms). The R_4 *t*-Bu amide of **3B** extends out toward the solvent exposed side of the active site, inducing a structural rearrangement of HKU4-CoV 3CL^{pro} where Gln192, which encloses **1A** and **2A** in the active site, is moved 2.7 Å to accommodate the steric bulk of the R_4 substituent of **3B**. The combination of these factors may be attributed for the observed 5-fold increase in IC_{50} when comparing **1A** and **2A** to **3B** and likely account for the reduced inhibitory activity of Class B compounds relative to Class A compounds.

The Class B peptidomimetic compounds were synthesized and tested for HKU4-CoV 3CL^{pro} inhibition as racemates, which may lead to significant differences in IC_{50} values. An example of this can be seen by the comparison of (*R*)-**13B** to racemic- and (*S*)-**13B** (Figure 4). The enantiopure (*R*)-**13B** has an IC_{50} of 9.3 ± 0.5 μM while the **13B** racemate has an IC_{50} of 11.1 ± 0.6 μM and (*S*)-**13B** has a 50% reduction in inhibition relative to the racemate, with only 44% inhibition of HKU4-CL^{pro} at 100 μM.. Interestingly, (*R*)-**3B** was found in the active site of HKU4-CoV 3CL^{pro} in the X-ray crystal structure (Figure 2, E and F), suggesting an (*R*)-stereochemical of the inhibitor for good inhibition of HKU4-CoV 3CL^{pro}, despite the nature of the R_1 and R_3 heterocyclic groups.

The X-ray structures of HKU4-CoV 3CL^{pro} in complex with inhibitors provide vital insights into the types of compounds that can be developed as therapeutics against lineage C *Betacoronaviruses.* A sequence alignment of HKU4-CoV, HKU5-CoV, and MERS-CoV 3CL^{pro}, all of which are lineage C *Betacoronaviruses*, show that HKU4-CoV and HKU5-CoV are 81.0% and 82.7% identical to MERS-CoV 3CL^{pro}, and HKU4-CoV is 83.7% identical to HKU5-CoV 3CL^{pro} (Figure 5).[31-33] Moreover, the pertinent HKU4-CoV 3CL^{pro} active site residues (Met25, His41, Cys44, Ala46, Tyr54, Cys148, His166,

Glu169, and Gln192, Figures 3 and 4) identified in the X-ray crystal structures that line the active site and interact with the peptidomimetic inhibitors are all conserved in HKU5-CoV and MERS-CoV 3CL^{pro}. These data indicate that the active site architectures among HKU4-CoV, HKU5-CoV, and MERS-CoV 3CL^{pro} may be similar enough to design broad-spectrum antiviral therapeutics against lineage C *Betacoronaviruses* and have implications for the structure and inhibition of lineage C *Betacoronaviruses* yet to emerge. To test this hypothesis, we tested whether our lead HKU4-CoV 3CL^{pro} inhibitor, compound **1A**, would also have inhibition of HKU5-CoV 3CL^{pro}. We found that compound **1A** is a good inhibitor of HKU5-CoV 3CL^{pro}, having 91% inhibition at 100 μM and a sub-micromolar IC_{50} value of 0.54 ± 0.03 μM which is comparable to the IC_{50} value of 0.33 ± 0.02 μM against HKU4-3CL^{pro}. Based on these data, we predict compound **1A** will show inhibition of MERS-CoV 3CL^{pro} as well.

3. Conclusions

In conclusion, 43 of the 230 peptidomimetics were found to inhibit HKU4-CoV 3CL^{pro}, 19 of which belonged to the Class A peptidomimetic series and 24 of which belonged to the Class B peptidomimetic series. Overall, the Class A peptidomimetics were found to be better inhibitors relative to the Class B compounds, and two of the Class A compounds were determined to have sub-micromolar inhibitory potency against HKU4-CoV 3CL^{pro}, **1A** and **2A**. Analysis of the inhibition data from the 230 peptidomimetics resulted in the identification of a favored inhibitor backbone consisting of 3-thiophene and 1-methylbenzotriazole functionalities. To evaluate the relative contribution of the favored inhibitor backbone to the total HKU4-CoV 3CL^{pro} inhibition observed for the molecule, we synthesized the sub-structural components of the lead inhibitor, **1A**, and tested them for inhibition of HKU4-CoV 3CL^{pro}. The simple compound, **22A**, which represents the R_1 and R_3 inhibitor functionalities and consists of the 3-thiophene and 1-methylbenzotriazole of the favored backbone, was found to inhibit HKU4-CoV 3CL^{pro} even in the absence of the anilido and R_2 components of the inhibitor. We then determined the X-ray crystal structures of the three most potent inhibitors containing this favored backbone, **1A**, **2A**, **3B,** in complex with HKU4-CoV 3CL^{pro}. These X-ray crystal structures prove that the three Class A and B inhibitors bind in the HKU4-CoV 3CL^{pro} active site, utilizing the same set of three hydrogen-bonding interactions between the favored backbone backbone and the HKU4-CoV 3CL^{pro} active site residues, serving to anchor compounds with this backbone into the active site of the enzyme. Our attempt to solve the X-ray structure of the privileged backbone compound, **22A**, in complex with HKU4-CoV 3CL^{pro} resulted in the structure of unbound HKU4-CoV 3CL^{pro}, which is presumably as a consequence of weak inhibition by **22A** (28% at 100

374 μM). Superposition of the unbound and inhibitor-bound forms of HKU4-CoV 3CL^{pro} revealed
375 several subtle, but important changes in the active site architecture upon inhibitor binding.
376 Furthermore, sequence alignment of HKU4-CoV, HKU5-CoV, and MERS-CoV 3CL^{pro} show that the
377 residues involved in inhibitor binding are conserved, indicating that identification of broad spectrum
378 3CL^{pro} inhibitors of lineage C *Betacoronaviruses* is possible. In support of this, we found our most
379 active HKU4-CoV 3CL^{pro} inhibitor to have inhibition of HKU5-CoV 3CL^{pro} in the sub-micromolar range
380 (IC_{50} = 0.54 ± 0.03 μM). These findings, and the structural details underlying the potent inhibition of
381 HKU4-CoV 3CL^{pro} by compounds containing 3-thiophene and 1-methylbenzotriazole backbones, can
382 be used in the future to design compounds with the ability to more fully exploit the HKU4-CoV 3CL^{pro}
383 active site, leading ultimately to the development of more highly potent and selective inhibitors
384 against human pathogens such as SARS and MERS.
385

386 **4. Experimental**

387 **4.1. Expression and purification of HKU4-CoV 3CL^{pro}**

388 The gene encoding the 3CL^{pro} of HKU4-CoV (residues 3292-3597 in the *Tylonycteris* bat-CoV
389 polyprotein)[9] was codon optimized for expression in *E. coli* and cloned into pET-11a expression
390 vector with an N-terminal $(His)_6$-tag followed by nsp4-/5 auto-cleavage site by BioBasic Inc. This
391 construct results in the expression of HKU4-CoV 3CL^{pro} without an N-terminal or C-terminal extension.
392 E. *coli* BL21(DE3) cells, transformed with pET11a-HKU4 3CL^{pro} plasmid were grown in Super LB
393 media (3 g potassium phosphate monobasic, 6 g sodium phosphate dibasic, 20 g tryptone, 5 g yeast
394 extracts, 5 g sodium in 1 L water, pH 7.2 adjusted with 1 M NaOH) in the presence of 1 mL 100
395 mg/mL carbenicillin, 25 mL 8% lactose, 10 mL 60% glycerol, and 5 mL of 10% glucose per 1 L of
396 expression culture for 24 hours at 25 °C. The cells were harvested by centrifugation (8,400 *g* for 20
397 min) to yield 15.5 g/L of cells. The cell pellet was then re-suspended in 5 mL of Buffer A/1 g cell
398 pellet (50 mM Tris pH 7.5, 0.2 M ammonium sulfate, 0.05 mM EDTA, 5 mM BME) containing 1 mg/mL
399 lysozyme. After the cells were homogenized, they were lysed via sonication for 10 minutes with 10 s
400 pulses at 50% amplitude using a Branson Digital Sonifier. The cell lysate was clarified by pelleting
401 the cell debris via centrifugation (28,960 *g*, 4 °C, 20 minutes) and loaded onto a 30 mL Phenyl
402 Sepharose 6 Fast Flow HiSub column equilibrated with Buffer A. Protein was eluted with a gradient
403 to 100% Buffer B (20 mM Tris pH 7.5, 0.05 mM EDTA, 5 mM BME) over five column volumes (150
404 mL) collecting 5 mL fractions. Fractions containing HKU4 3CL^{pro} were pooled and loaded onto a 60
405 mL DEAE Sepharose Fast Flow column equilibrated with Buffer B. Protein was eluted with a gradient
406 to 50% Buffer C (50 mM Tris pH 7.5, 1 M sodium chloride, 0.05 mM EDTA, 5 mM BME, 10% glycerol)
407 over five column volumes (300 mL) collecting 5 mL fractions. Fractions containing pure HKU4-CoV

408 3CL^{pro} were pooled, dialized into storage buffer (25 mM HEPES, pH 7.5, 2.5 mM DTT, 10%
409 glycerol), and concentrated. The protein was then aliquoted into 1.5 mL push-cap Eppendorf tubes,
410 flash frozen in liquid nitrogen, and stored at -80 ℃ in a freezer until further use.
411

412 **4.2. IC_{50} Determination of inhibitors against HKU4-CoV 3CL^{pro} at 25 ℃ and 37 ℃:**

413 Each of the 230 dipeptide-like inhibitors were first screened for inhibition of HKU4 3CL^{pro} at a
414 concentration of 100 μM in duplicate assays containing the following assay buffer (50 mM HEPES,
415 0.1 mg/mL BSA, 0.01% TritonX-100, 1 mM DTT). The assays were carried out in Costar 3694
416 EIA/RIA 96-Well Half Area, Flat Bottom, Black Polystyrene plates from Corning Incorporated. 1 μL of
417 100X inhibitor stock in DMSO was added to 79 μL of enzyme in assay buffer and the enzyme-inhibitor
418 mixture was incubated for 10 minutes. The reaction was initiated by the addition of 20 μL of 10 μM
419 UIVT3 substrate, a custom synthesized Förster resonance energy transfer substrate peptide with the
420 following sequence: HilyteFluor™488-ESARLQSGLRKAK-QXL520™-NH_2, producing final
421 concentrations of 100 nM and 100 μM for the 3CL^{pro} enzyme and UIVT3 substrate, respectively. The
422 fluorescence intensity of the reaction was then measured over time as relative fluorescence units
423 (RFU_t) for a period of 10 minutes, using an excitation wavelength of 485 and bandwidth of 20 nm and
424 monitoring emission at 528 and bandwidth of 20 nm using a BioTek Synergy H1 multimode
425 microplate reader.

426 The inhibition of HKU4-CoV 3CL^{pro} by inhibitor compounds was monitored by following the
427 change in RFUs over time, using the initial slope of the progress curve to determine the initial rate
428 (V_i). The percent inhibition of the 3CL^{pro} enzymes was determined using the following equation:
429

$$\%\,Inhibition = \left[1 - \frac{Inhibited\ 3CLpro\ RFU/s - Background\ RFU/s}{Uninhibited\ 3CLpro\ RFU/s - Background\ RFU/s}\right] * 100$$

430

431 Full IC_{50} data were acquired for the compounds that showed greater than 50% inhibition of
432 HKU4-CoV 3CL^{pro} at 100 μM of inhibitor compound. The IC_{50} values were determined at ambient
433 temperature from 100 μL assays performed in triplicate in the following buffer: 50 mM HEPES, 0.1
434 mg/mL BSA, 0.01% TritonX-100, 1 mM DTT. Kinetic assays were carried out in Costar 3694 EIA/RIA
435 96-Well Half Area, Flat Bottom, Black Polystyrene plates from Corning Incorporated. Each inhibitor
436 was tested at concentrations of 0.313, 0.652, 1.25, 2.5, 5.0, 10.0, 20.0, 40.0, 60.0, 80.0, 100.0, and
437 120.0 μM; 1 μL of 100X inhibitor stock in DMSO was added to 79 μL of enzyme in assay buffer and
438 the enzyme-inhibitor mixture was incubated for 10 minutes. The reaction was initiated by the addition
439 of 20 μL of 10 μM UIVT3 substrate, producing final concentrations of 100 nM and 2 μM for the 3CL^{pro}

enzyme and UIVT3 substrate, respectively. The fluorescence intensity of the reaction was then measured over time as RFU_t for a period of 20 minutes, using an excitation wavelength of 485 and bandwidth of 20 nm and monitoring emission at 528 and bandwidth of 20 nm using a BioTek Synergy H1 multimode microplate reader.

The percent inhibition of the $3CL^{pro}$ enzymes was then plotted as a function of inhibitor concentration. The SigmaPlot Enzyme Kinetics Wizard was used to fit the triplicate percent inhibition data and associated standard error to a non-linear Michaelis-Menten type regression model and determine the IC_{50} for each enzyme using the following equation:

$$\%\,Inhibition = \frac{\%I_{max} * [\text{Inhibitor}]}{\text{IC}_{5o} + [\text{Inhibitor}]}$$

where $\%I_{max}$ is the percent maximum inhibition of $3CL^{pro}$ and the error in IC_{50} values was determined as the error in the fitted parameter.

4.3. Crystallization and X-ray structure determination of HKU4 3C-like protease in complex with inhibitors:

The HKU4 $3CL^{pro}$-inhibitor complexes were co-crystallized from four different crystallization solutions. Briefly, the hanging-drop, vapor-diffusion method was used for crystallization by setting up drops and adding 1 µL of purified HKU4-CoV $3CL^{pro}$ (2.5 mg/mL, 75 µM), that had been incubated for three hours with a 3 molar excess of the appropriate inhibitor, and 1 µL of reservoir solution. For **1A**: 15% PEG-3350, 2% tacsimate, 5% isopropanol, 0.1 M imidazole pH 6; for **3B**: 20% PEG-3350, 0.2 M ammonium acetate, 0.1 M Bis-Tris pH 5.5; for **2A**: 18% PEG-3350, 5% tacsimate, 0.2 M ammonium sulfate, 0.1 M Bis-Tris pH5.5; for **22A**: 10% PEG-3350, 2% tacsimate, 5% isopropanol, 0.1 M imidazole pH 6.5. Protein crystals appeared between 14 hours and 7 days after setting up crystallization plates. Crystals were harvested with a nylon loop, which was then swiped through the same mother-liquor solution supplemented with 15% MPD. The crystals were cooled by plunging into liquid nitrogen and stored in shipping dewars containing liquid nitrogen until X-ray data collection at an available synchrotron could be performed.

All diffraction data were collected at 100 K at the Life Sciences Collaborative Access Team (LS-CAT) at the Advanced Photon Source (APS) at Argonne National Laboratories. Crystals were transferred from shipping dewars into automated dewars and then and mounted robotically on a goniostat while under a stream of N_2. X-ray data sets of HKU4 $3CL^{pro}$-inhibitor complexes were collected on a Rayonix 225 HE detector at a wavelength of 0.98 Å. X-ray data were processed and

scaled using the program HLK2000, crystals of HKU4-CoV 3CL^{pro} complexes with the inhibitors **1A**, **2A**, and **3B** belonged to the space group $P2_12_12_1$, and HKU4-CoV 3CL^{pro} crystallized as a dimer in the asymmetric unit. Co-crystallization of HKU4-CoV 3CL^{pro} with **22A** did not result in an HKU4-CoV 3CL^{pro}:inhibitor co-complex, but instead yielded the apo form of HKU4-CoV 3CL^{pro}, which crystallized in a different space group, $P3_121$ with one dimer per asymmetric unit.

The initial phases for HKU4-CoV 3CL^{pro} in complex with **1A**, **2A**, and **3B** were determined by molecular replacement using Phaser-MR (simple interface) in the Phenix suite and the protein database PDB file 2YNA.[34] The inhibitors were built and optimized from their SMILES strings using eLBOW and fit into the density using LigandFit in the Phenix suite and the program COOT. Structures were refined using Phenix. Water molecules were added manually to the $2F_o$-F_c density peaks that were greater than 3.0 and iterative rounds of refinement were carried out until R_{work} and R_{free} reached their lowest values. The electron density maps presented in the figures were calculated using Phenix and COOT and the figures generated using the program PyMol.

4.4. General chemistry methods

All reagents and chemicals were purchased from SigmaAldrich or Acros Organics and used without further purification. Anhydrous solvents were purchased or purified by passage through a solvent column composed of activated alumina and a supported copper redox catalyst. Analytical thin-layer chromatography was performed using Sorbent Technologies Glass-Backed Silica Gel HL TLC plates w/UV254. Flash chromatography was performed with Sorbent Technologies 200-400 mesh silica gel. Nuclear magnetic resonance (NMR) data was acquired using either a Varian Inova300, Bruker ARX400, or Bruker AV-III-800 spectrometers at 300, 400, or 800 MHz for ^{1}H or 75, 100, or 200 MHz for ^{13}C. All compounds were purified by flash chromatography to >90% purity by ^{1}H NMR.

2-(1*H*-benzo[*d*][1,2,3]triazol-1-yl)-*N*-(thiophen-3-ylmethyl)acetamide (22A).

To 2-(1*H*-benzo[*d*][1,2,3]triazol-1-yl)acetic acid (1.5 eq.) in anhydrous dichloromethane (0.2 M) at 0 °C under nitrogen atmosphere was added EDC (3.0 eq.) and HOBT (3.0 eq.). The mixture was allowed to stir for five minutes before the addition of DIEA (13.0 eq.). The mixture was allowed to stir for an additional 20 minutes before the addition of thiophen-3-ylmethanamine (1.0 eq.). The reaction mixture was allowed to warm to ambient temperature and stirred under nitrogen atmosphere for 16 hours. The reaction was quenched by addition of saturated potassium bicarbonate and the aqueous layer was extracted with ethyl acetate (3X). The combined organic layers were washed with water (1X) and brine (1X), dried over sodium sulfate, and concentrated. The crude residue was

recrystallized from hot ethanol to provide the product as a beautiful white, crystalline solid in 30% yield. ^{1}H NMR (800 MHz, CD_3OD) (ppm): 8.03 (1H, d, J = 8.37), 7.72 (1H, d, J = 8.37), 7.59 (1H, dd, J = 8.37, 0.96), 7.48 (1H, dd, J = 8.37, 0.96), 7.40 (1H, dd, J = 4.94, 2.97), 7.29 (1H, m), 7.08 (1H, dd, J = 4.93, 1.30), 5.51 (2H, s), 4.46 (2H, s). ^{13}C NMR (200 MHz, CD_3OD) (ppm): 166.47, 145.30, 138.67, 133.83, 127.63, 126.92, 125.81, 124.28, 121.90, 118.60, 110.11, 49.87, 38.19. ESI-MS(+): 273 [M + 1], 295 [M + 23].

***N*-(4-aminophenyl)thiophene-2-carboxamide (23A).**

Thiophene-2-carboxylic acid (1.0 eq.) and HATU (1.4 eq.) were added to anhydrous dichloromethane (0.2 M) at room temperature followed by drop-wise addition of DIEA (3.0 eq.) under nitrogen atmosphere. The mixture was allowed to stir at ambient temperature for 5 minutes before benzene-1,4-diamine was added in one portion. The reaction mixture was allowed to stir for 14 hours before it was quenched with saturated potassium bicarbonate. The aqueous layer was extracted with ethyl acetate (3X) and the combined organic extracts were washed with water (1X) and brine (1X), dried over sodium sulfate, and concentrated. The crude yellow residue was purified by flash chromatography using a gradient of 20% to 70% ethyl acetate in hexanes to give the final product in 50% yield. This reaction was performed from mg to g scale with no detrimental effect on yield. ^{1}H NMR (800 MHz, CD_3OD) (ppm): 7.84 (1H, d, J = 3.74), 7.67 (1H, dd, J = 4.97, 1.08), 7.37 (2H, d, J = 8.56), 7.15 (1H, dd, J = 4.97, 3.74). ^{13}C NMR (200 MHz, CD_3OD) (ppm): 161.26, 144.66, 139.63, 130.56, 128.71, 128.31, 127.49, 122.85. ESI-MS(+): 219 [M + 1], 241 [M + 23].

***N*-(4-((thiophen-3-ylmethyl)amino)phenyl)thiophene-2-carboxamide (24A).**

23A (1.0 eq.) and thiophene-3-carbaldehyde (1.0 eq.) were dissolved in anhydrous 1,2-DCE (0.2 M) at ambient temperature under nitrogen atmosphere. Sodium triacetoxyborohydride (1.6 eq.) and acetic acid (1.0 eq.) were then added in one portion. The reaction mixture was allowed to stir for 30 minutes before the reaction was quenched with 1 N sodium hydroxide. The aqueous layer was extracted with ethyl acetate (3X) and the combined organic extracts were washed with water (1X) and brine (1X), dried over sodium sulfate, and concentrated. The crude yellow residue was purified by flash chromatography using a gradient of 20% to 70% ethyl acetate in hexanes to give the final product in 50-80% yield. ^{1}H NMR (800 MHz, CD_3OD) (ppm): 7.85 (1H, m), 7.69 (1H, m), 7.36 (3H, m), 7.26 (1H, m), 7.17 (1H, d, J = 5.15), 7.12 (1H, d, J = 5.15), 6.70 (2H, m), 4.34-4.35 (2H, rotomeric peaks). ^{13}C NMR (200 MHz, CD_3OD) (ppm): 172.76, 146.24, 141.08, 130.47, 128.20, 127.65, 127.43, 126.82, 125.27, 122.87, 120.85, 112.81, 43.08). ESI-MS(+): 315 [M + 1], 337 [M + 23].

5. Author Contributions

Sarah E. St. John (SSJ) expressed, purified, and characterized HKU4-3CL^{pro}. SSJ designed and performed all of the experiments and synthesis detailed herein and was responsible for crystallizing unbound and bound HKU4-3CL^{pro}:inhibitor complexes and solving their X-ray structures. SSJ wrote the research article and made all figures/schemes/tables. Sakshi Tomar (ST) designed the HKU4- and HKU5-3CL^{pro} expression plasmids, and over expressed and purified the HKU5-3CL^{pro} enzyme and tested for inhibition by **1A**. The original compound library (S1 and S2) was synthesized in the laboratory of Shaun R. Stauffer (SRS), who also edited this article. Andrew D. Mesecar (ADM) supervised this research study.

6. Acknowledgements

This work was supported in part by grants (AI085089 and AI26603) to ADM from the National Institutes of Health via the National Institute of Allergy and Infectious Diseases. ADM also wishes to also acknowledge partial support from the Walther Cancer Foundation. Sakshi Tomar is supported by a grant from the Purdue University Research Foundation. Crystallization and DNA sequencing were partially supported by the Purdue Center for Cancer Research Macromolecular Crystallography and DNA Sequencing Shared Resources which are partially supported by an NIH grant (P30 CA023168). The authors would also like to acknowledge the scientists at the Vanderbilt Specialized Chemistry Center for synthesis of the initial compound library used in this work, which was supported in part by the MLPCN (1U54 MH084659 and MH084512). Finally, the authors would like to acknowledge the LS-CAT beamline staff for their help in acquiring X-ray data. Use of the Advanced Photon Source, an Office of Science User Facility operated for the U.S. Department of Energy (DOE) Office of Science by Argonne National Laboratory, was supported by the U.S. DOE under Contract No. DE-AC02-06CH11357. Use of the LS-CAT Sector 21 was supported by the Michigan Economic Development Corporation and the Michigan Technology Tri-Corridor (Grant 085P1000817).

6. References

(1) McIntosh, K.; Dees, J. H.; Becker, W. B.; Kapikian, A. Z.; Chanock, R. M. *Proceedings of the National Academy of Sciences of the United States of America* **1967**, *57*, 933.

(2) Greenblatt, M. B.; Vrbanac, V.; Tivey, T.; Tsang, K.; Tager, A. M.; Aliprantis, A. O. *PLoS One* **2012**, *7*, e44664.

(3) Perlman, S.; Netland, J. *Nature reviews. Microbiology* **2009**, *7*, 439.

(4) Ksiazek, T. G.; Erdman, D.; Goldsmith, C. S.; Zaki, S. R.; Peret, T.; Emery, S.; Tong, S.; Urbani, C.; Comer, J. A.; Lim, W.; Rollin, P. E.; Dowell, S. F.; Ling, A. E.; Humphrey, C. D.; Shieh, W. J.; Guarner, J.; Paddock, C. D.; Rota, P.; Fields, B.; DeRisi, J.; Yang, J. Y.; Cox, N.; Hughes, J. M.; LeDuc, J. W.; Bellini, W. J.; Anderson, L. J. *N Engl J Med* **2003**, *348*, 1953.

(5) Drosten, C.; Gunther, S.; Preiser, W.; van der Werf, S.; Brodt, H. R.; Becker, S.; Rabenau, H.; Panning, M.; Kolesnikova, L.; Fouchier, R. A.; Berger, A.; Burguiere, A. M.; Cinatl, J.; Eickmann, M.; Escriou, N.; Grywna, K.; Kramme, S.; Manuguerra, J. C.; Muller, S.; Rickerts, V.; Sturmer, M.; Vieth, S.; Klenk, H. D.; Osterhaus, A. D.; Schmitz, H.; Doerr, H. W. *N Engl J Med* **2003**, *348*, 1967.

(6) Chan, J. F.; Lau, S. K.; Woo, P. C. *J Formos Med Assoc* **2013**, *112*, 372.

(7) Zaki, A. M.; van Boheemen, S.; Bestebroer, T. M.; Osterhaus, A. D.; Fouchier, R. A. *N Engl J Med* **2012**, *367*, 1814.

(8) WHO In *MERS-CoV Update 16*; World Health Organization: 2014; Vol. 2014.

(9) Woo, P. C.; Wang, M.; Lau, S. K.; Xu, H.; Poon, R. W.; Guo, R.; Wong, B. H.; Gao, K.; Tsoi, H. W.; Huang, Y.; Li, K. S.; Lam, C. S.; Chan, K. H.; Zheng, B. J.; Yuen, K. Y. *Journal of virology* **2007**, *81*, 1574.

(10) de Groot, R. J.; Baker, S. C.; Baric, R. S.; Brown, C. S.; Drosten, C.; Enjuanes, L.; Fouchier, R. A.; Galiano, M.; Gorbalenya, A. E.; Memish, Z. A.; Perlman, S.; Poon, L. L.; Snijder, E. J.; Stephens, G. M.; Woo, P. C.; Zaki, A. M.; Zambon, M.; Ziebuhr, J. *Journal of virology* **2013**, *87*, 7790.

(11) van Boheemen, S.; de Graaf, M.; Lauber, C.; Bestebroer, T. M.; Raj, V. S.; Zaki, A. M.; Osterhaus, A. D.; Haagmans, B. L.; Gorbalenya, A. E.; Snijder, E. J.; Fouchier, R. A. *MBio* **2012**, *3*.

(12) Haagmans, B. L. A. D., S.H.S.; Reusken, C.B.E.M; Raj, V.S.; Galiano, M.G.; Myers, R.; Godeke G.J.; Jonges, M.; Farag, E.; Diab, A.; Ghobashy, H.; Alhajri, F.; Al-Thani, M.; Al-Marri, S.A.; Al Romaihi, H.E.; Al Khal, A.; Bermingham, A.; Osterhaus, A.D.M.E; Al Hajri, M.M.; Koopmans, M.P.G. *The Lancet Infectious Diseases* **2014**, *14*, 140.

(13) Memish, Z. A.; Mishra, N.; Olival, K. J.; Fagbo, S. F.; Kapoor, V.; Epstein, J. H.; Alhakeem, R.; Durosinloun, A.; Al Asmari, M.; Islam, A.; Kapoor, A.; Briese, T.; Daszak, P.; Al Rabeeah, A. A.; Lipkin, W. I. *Emerging infectious diseases* **2013**, *19*, 1819.

(14) Niemeyer, D.; Zillinger, T.; Muth, D.; Zielecki, F.; Horvath, G.; Suliman, T.; Barchet, W.; Weber, F.; Drosten, C.; Muller, M. A. *Journal of virology* **2013**, *87*, 12489.

(15) Matthews, K. L.; Coleman, C. M.; van der Meer, Y.; Snijder, E. J.; Frieman, M. B. *J Gen Virol* **2014**, *95*, 874.

(16) Wang, Q. H.; Qi, J. X.; Yuan, Y.; Xuan, Y. F.; Han, P. C.; Wan, Y. H.; Ji, W.; Li, Y.; Wu, Y.; Wang, J. W.; Iwamoto, A.; Woo, P. C. Y.; Yuen, K. Y.; Yan, J. H.; Lu, G. W.; Gao, G. F. *Cell Host & Microbe* **2014**, *16*, 328.

(17) Gorbalenya, A. E.; Enjuanes, L.; Ziebuhr, J.; Snijder, E. J. *Virus research* **2006**, *117*, 17.

(18) Snijder, E. J.; Bredenbeek, P. J.; Dobbe, J. C.; Thiel, V.; Ziebuhr, J.; Poon, L. L.; Guan, Y.; Rozanov, M.; Spaan, W. J.; Gorbalenya, A. E. *Journal of molecular biology* **2003**, *331*, 991.

(19) Ziebuhr, J.; Snijder, E. J.; Gorbalenya, A. E. *J Gen Virol* **2000**, *81*, 853.

(20) Thiel, V.; Ivanov, K. A.; Putics, A.; Hertzig, T.; Schelle, B.; Bayer, S.; Weissbrich, B.; Snijder, E. J.; Rabenau, H.; Doerr, H. W.; Gorbalenya, A. E.; Ziebuhr, J. *J Gen Virol* **2003**, *84*, 2305.

(21) Anand, K.; Ziebuhr, J.; Wadhwani, P.; Mesters, J. R.; Hilgenfeld, R. *Science* **2003**, *300*, 1763.

(22) Thiel, V.; Herold, J.; Schelle, B.; Siddell, S. G. *Journal of virology* **2001**, *75*, 6676.

(23) Jacobs, J.; Grum-Tokars, V.; Zhou, Y.; Turlington, M.; Saldanha, S. A.; Chase, P.; Eggler, A.; Dawson, E. S.; Baez-Santos, Y. M.; Tomar, S.; Mielech, A. M.; Baker, S. C.; Lindsley, C. W.; Hodder, P.; Mesecar, A.; Stauffer, S. R. *Journal of Medicinal Chemistry* **2013**, *56*, 534.

(24) Turlington, M.; Chun, A.; Tomar, S.; Eggler, A.; Grum-Tokars, V.; Jacobs, J.; Daniels, J. S.; Dawson, E.; Saldanha, A.; Chase, P.; Baez-Santos, Y. M.; Lindsley, C. W.; Hodder, P.; Mesecar, A. D.; Stauffer, S. R. *Bioorganic & Medicinal Chemistry Letters* **2013**, *23*, 6172.

(25) Rajput, A. P. G., R.P. *Journal of Chemical and Pharmaceutical Research* **2010**, *2*, 52.

(26) Wu, C. Y.; King, K. Y.; Kuo, C. J.; Fang, J. M.; Wu, Y. T.; Ho, M. Y.; Liao, C. L.; Shie, J. J.; Liang, P. H.; Wong, C. H. *Chem Biol* **2006**, *13*, 261.

(27) Cooke, S. A.; Corlett, G. K.; Legon, A. C. *Chem Phys Lett* **1998**, *291*, 269.
(28) Cooke, S. A.; Corlett, G. K.; Legon, A. C. *J Chem Soc Faraday T* **1998**, *94*, 1565.
(29) Laurence, C.; Brameld, K. A.; Graton, J.; Le Questel, J. Y.; Renault, E. *Journal of Medicinal Chemistry* **2009**, *52*, 4073.
(30) Legon, A. C.; Ottaviani, P. *Physical Chemistry Chemical Physics* **2004**, *6*, 488.
(31) Gouet, P.; Robert, X.; Courcelle, E. *Nucleic Acids Research* **2003**, *31*, 3320.
(32) Gouet, P.; Courcelle, E.; Stuart, D. I.; Metoz, F. *Bioinformatics* **1999**, *15*, 305.
(33) Cockerill, M. *Trends Biochem Sci* **1993**, *18*, 106.
(34) Adams, P. D.; Afonine, P. V.; Bunkoczi, G.; Chen, V. B.; Davis, I. W.; Echols, N.; Headd, J. J.; Hung, L. W.; Kapral, G. J.; Grosse-Kunstleve, R. W.; McCoy, A. J.; Moriarty, N. W.; Oeffner, R.; Read, R. J.; Richardson, D. C.; Richardson, J. S.; Terwilliger, T. C.; Zwart, P. H. *Acta Crystallogr D* **2010**, *66*, 213.

7. Figure Legends

Figure 1. Genome and proteome organization of HKU4-, HKU5-, and MERS-CoV non-structural proteins highlighting the PLpro and 3CL-pro cleavage sites.

Figure 2. X-ray crystal structures of **1A**, **2A** and **3B** in complex with HKU4-CoV 3CL^{pro}. Inhibitors are colored according to atom type and shown in ball and stick representation. Wall-eye stereo-view is shown in panels A, C, and E. Water molecules are shown as red spheres. Hydrogen bonds are shown as gray dashes with distances between heteroatoms labeled (Å). Interatomic distances (Å) are displayed using a gray arrow. Electron density omit maps ($F_o - F_c$) are shown in grey mesh and are contoured to +3.0 around the inhibitor only. The binding orientation of each inhibitor is the same in the active site of each monomer of the dimer in the asymmetric unit of HKU4-CoV 3CL^{pro}, therefore only one active site is shown for clarity. (A) HKU4-CoV 3CL^{pro} (pale yellow) in complex with **1A** (sky blue), PDB 4YOI, (B) **1A** electron density omit map, (C) HKU4-CoV 3CL^{pro} (wheat) in complex with **2A** (pale cyan), PDB 4YOJ, (D) **2A** electron density omit map, (E) HKU4-CoV 3CL^{pro} (light orange) in complex with **3B** (slate), PDB 4YOG, (F) **3B** electron density omit map contoured at +3.0 (blue) and +2.0 (grey).

Figure 3. (A) Superposition of unbound HKU4-CoV 3CL^{pro} (gray, PDB 4YO9) and HKU4-CoV 3CL^{pro} co-crystallized with inhibitor **1A** (where HKU4-CoV 3CL^{pro} is shown in ribbon representation in light yellow and **1A** is shown in sky blue and colored by element, PDB 4YOI). The Zn atom in the unbound HKU4-CoV 3CL^{pro} is represented as a gray sphere. (B) Superposition of HKU4-CoV 3CL^{pro} co-crystallized with **1A** (where HKU4-CoV 3CL^{pro} is shown in ribbon representation in light yellow and **1A** is shown in sky blue and colored by element, PDB 4YOI) and HKU4-CoV 3CL^{pro} co-crystallized with **2A** (where HKU4-CoV 3CL^{pro} is shown as cartoon in wheat and **2A** is shown in pale cyan and colored by element, PDB 4YOJ). (C) Superposition of HKU4-CoV 3CL^{pro} co-crystallized with **1A** (where HKU4-CoV 3CL^{pro} is shown in ribbon representation in light yellow and **1A** is shown in sky blue and colored by element, PDB 4YOI) and HKU4-CoV 3CL^{pro} co-crystallized with **3B** (where HKU4-CoV 3CL^{pro} is shown as cartoon in light orange and **3B** is shown in slate and colored by element, PDB 4YOG). Wall-eye stereo-view is shown in each panel.

Figure 4. Effect of **13B** stereocenter configuration on HKU4-CoV 3CL^{pro} inhibition. Where % inhibition is determined at 100 μM inhibition concentration, n/t = not tested.

Figure 5. Sequence alignment of HKU4-CoV, HKU5-CoV, and MERS-CoV 3CL^{pro} where the top row indicates the secondary structure of HKU4-3CLpro at a particular residue position, conserved

residues among all three 3CL^{pro}'s are shaded in red, and residues that have similar steric or electronic properties are shown in red text with no shading. Non-conserved residues are displayed in black text. The pertinent active site residues that border and interact with the peptidomimetic inhibitors (Met25, His41, Cys44, Ala46, Tyr54, Cys148, His166, Glu169, and Gln192) are indicated by blue arrows.

8. Scheme Legends

Scheme 1. Synthesis of sub-structural components of **1A**.

9. Tables

Table 1a. Class A peptidomimetic inhibitors.

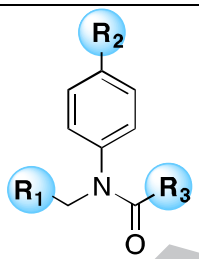

Peptidomimetic Backbone 1 (Class A)

Cmpd.	R_1	R_2	R_3	IC_{50} (μM)
1A		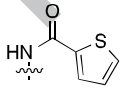	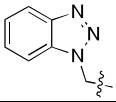	0.33 ± 0.02
2A		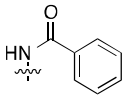	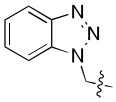	0.41 ± 0.04
3A		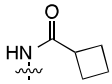	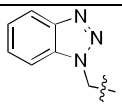	1.2 ± 0.2
4A		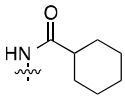	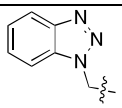	1.2 ± 0.06
5A			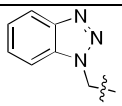	1.5 ± 0.1
6A		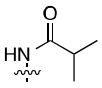	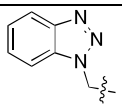	1.6 ± 0.09
7A			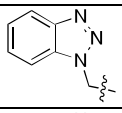	1.7 ± 0.2
8A		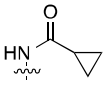	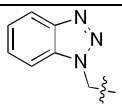	1.9 ± 0.09
9A		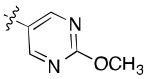	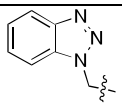	2.0 ± 0.2

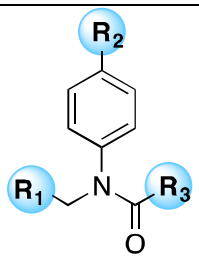

Peptidomimetic Backbone 1
(Class A)

Cmpd.	R_1	R_2	R_3	IC_{50} (μM)
10A		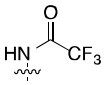	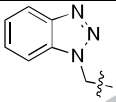	2.2 ± 0.2
11A			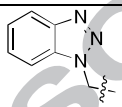	2.4 ± 0.3
12A		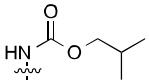	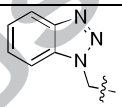	2.8 ± 0.4
13A		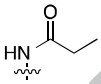	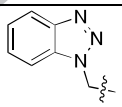	3.1 ± 0.3
14A		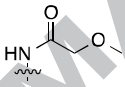	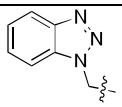	3.1 ± 0.3
15A		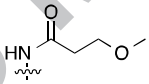	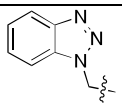	3.7 ± 0.4
16A			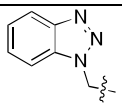	4.8 ± 0.4
17A		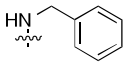	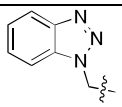	5.3 ± 0.6
18A		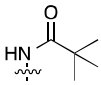	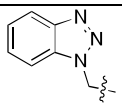	8.8 ± 0.8
19A		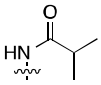	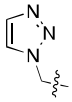	16.0 ± 4.0

Table 1b. Class B peptidomimetic inhibitors.

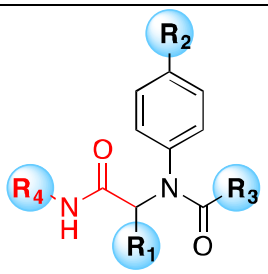

Peptidomimetic Backbone 2
(B Class)

Cmpd.	R_1	R_2	R_3	R_4	IC_{50} (μM)
1B					1.3 ± 0.3
2B	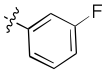	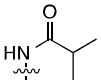	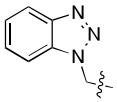	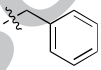	1.5 ± 0.3
3B			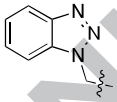		1.8 ± 0.5
4B					2.2 ± 0.6
5B			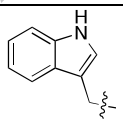		2.2 ± 0.4
6B		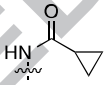	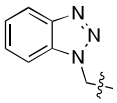		2.7 ± 0.4
7B	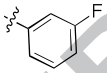	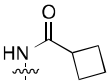	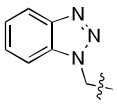	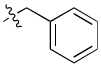	3.4 ± 0.4
8B			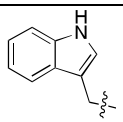		3.9 ± 0.7
9B		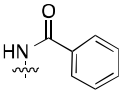	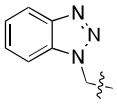		4.2 ± 0.2
10B			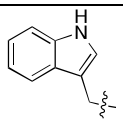		6.9 ± 0.7
11B	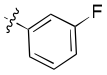	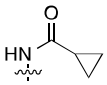	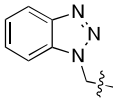	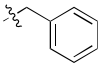	7.0 ± 1.2
12B					8.6 ± 0.9

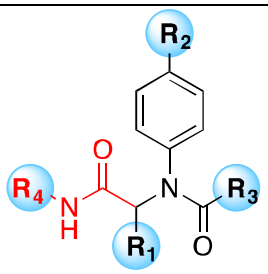

Peptidomimetic Backbone 2
(B Class)

Cmpd.	R_1	R_2	R_3	R_4	IC_{50} (μM)
13B					9.3 ± 0.5
14B					9.5 ± 2.0
15B					11.1 ± 0.6
16B		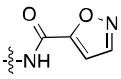	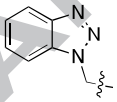		14.7 ± 1.1
17B					15.4 ± 2.1
18B		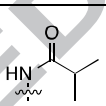	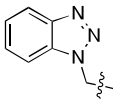		17.2 ± 2.8
19B		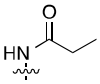	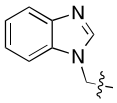		18.3 ± 4.7
20B	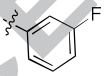		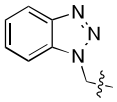		18.7 ± 2.6
21B			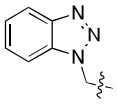		22.0 ± 7.4
22B					35.6 ± 5.2
23B		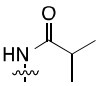	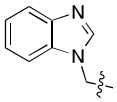		52.3 ± 21.2
24B					55.6 ± 14.3

Figure 1

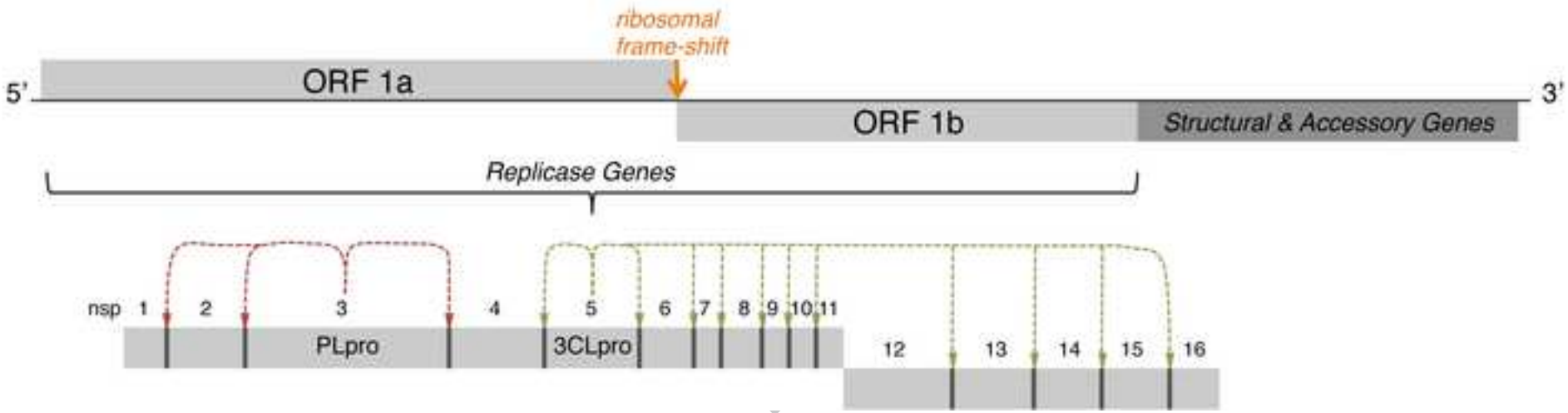

Figure 2

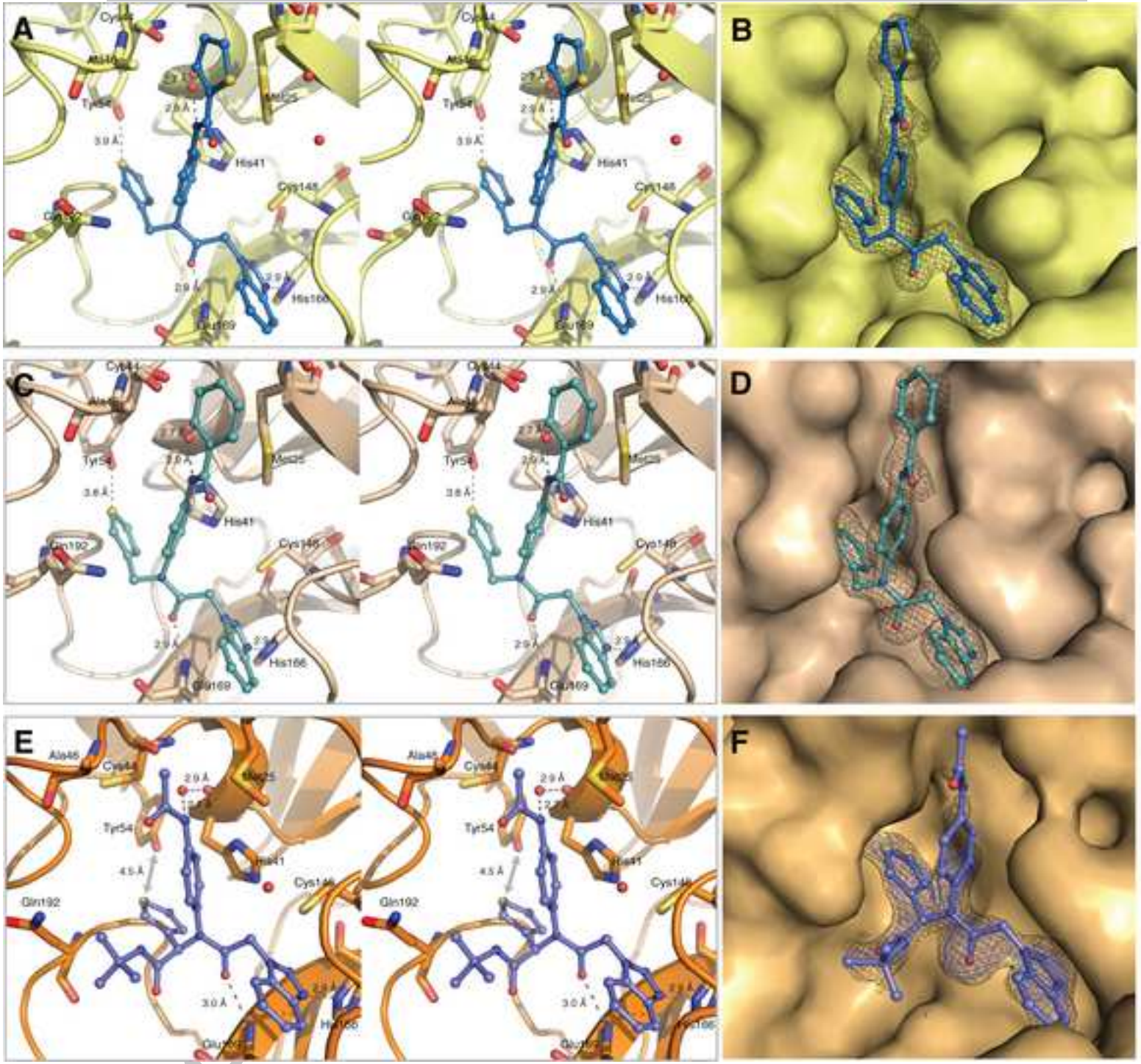

Figure 3

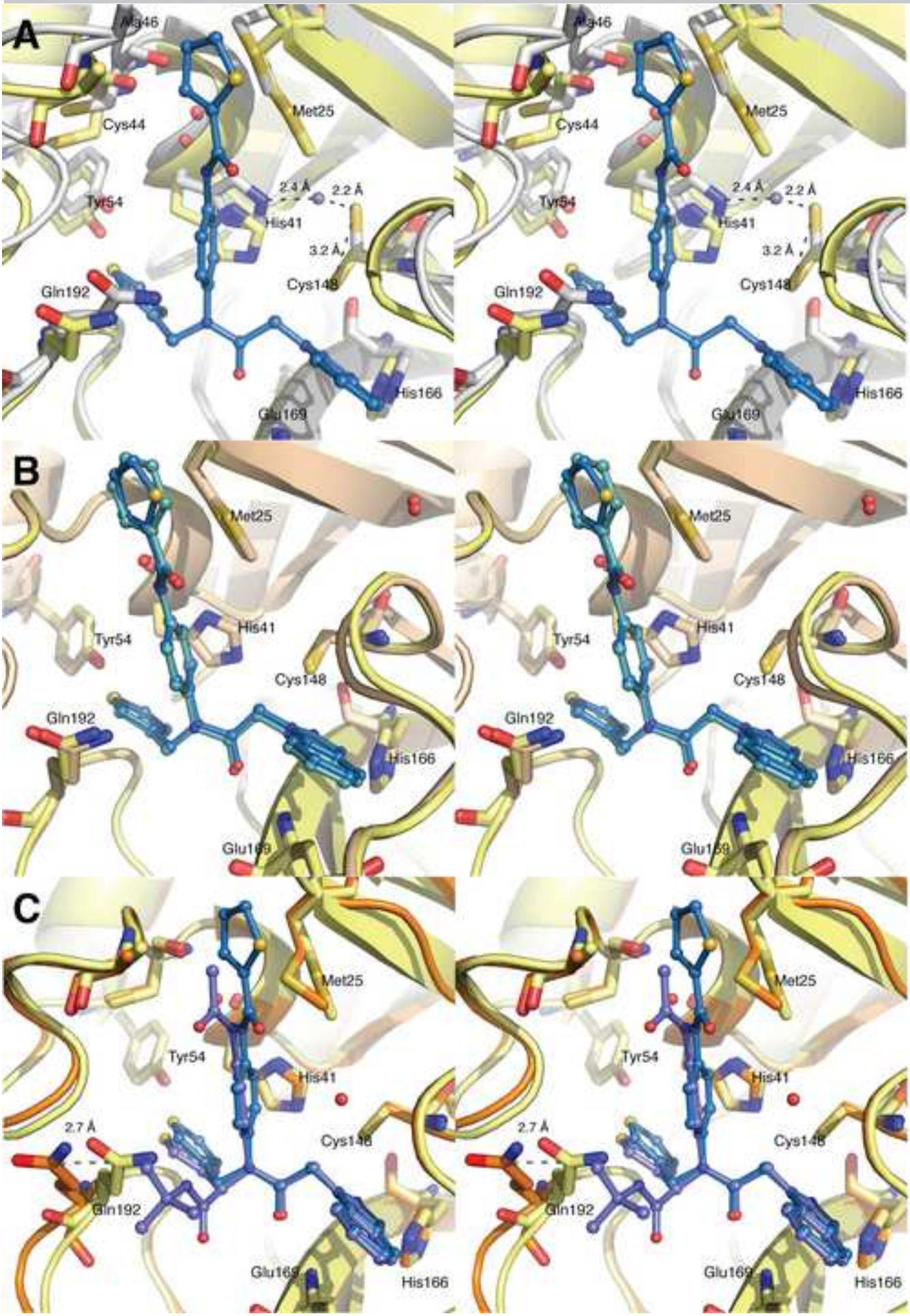

Figure 4

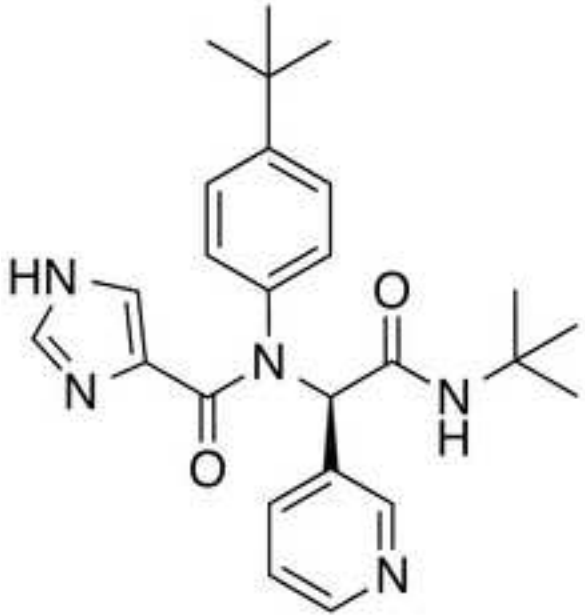

(*R*)-13B
93% Inhibition
$IC_{50} = 9.3 \pm 0.5\ \mu M$

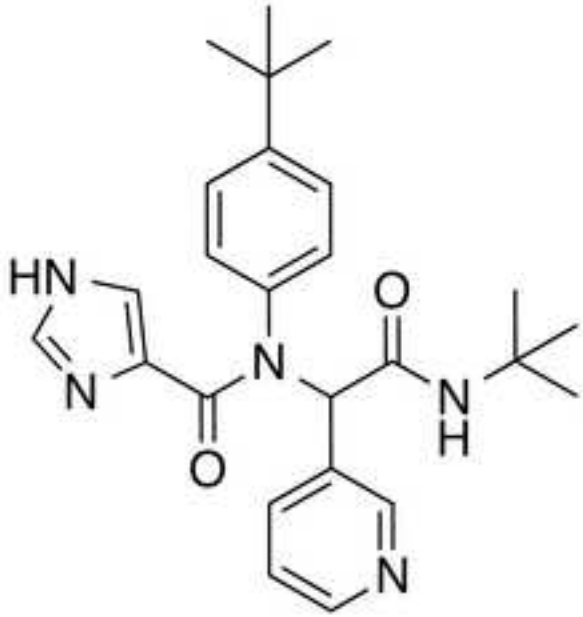

racemic-13B
94% Inhibition
$IC_{50} = 11.1 \pm 0.6\ \mu M$

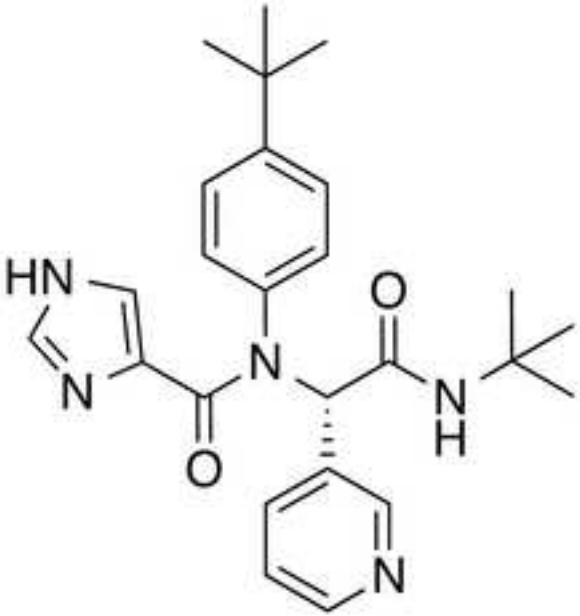

(*S*)-13B
44% Inhibition
$IC_{50} = n/t$

Figure 5

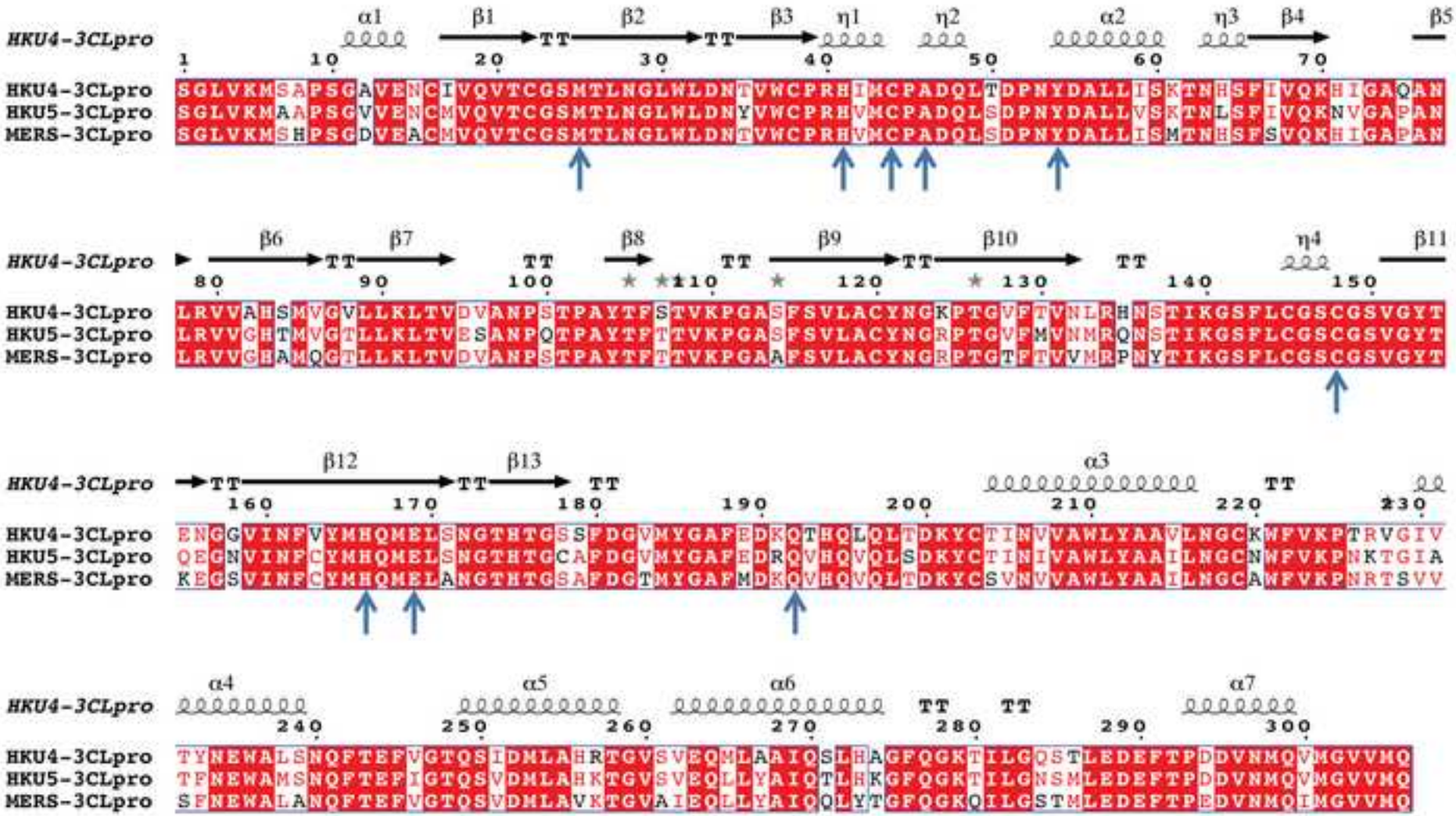

Scheme 1